The Astrophysical Journal, 866:21 (14pp), 2018 October 10 https://doi.org/10.3847/1538-4357/aadfd6

The White Dwarf Initial–Final Mass Relation for Progenitor Stars from 0.85 to 7.5 $M_{\odot}$*

Jeffrey D. Cummings[1], Jason S. Kalirai[1,2], P.-E. Tremblay[3], Enrico Ramirez-Ruiz[4], and Jieun Choi[5]
[1] Center for Astrophysical Sciences, Johns Hopkins University, 3400 N. Charles Street, Baltimore, MD 21218, USA; jcummi19@jhu.edu
[2] Space Telescope Science Institute, 3700 San Martin Drive, Baltimore, MD 21218, USA; jkalirai@stsci.edu
[3] Department of Physics, University of Warwick, Coventry CV4 7AL, UK; P-E.Tremblay@warwick.ac.uk
[4] Department of Astronomy and Astrophysics, University of California, Santa Cruz, CA 95064, USA; enrico@ucolick.org
[5] Harvard-Smithsonian Center for Astrophysics, Cambridge, MA 02138, USA; jieun.choi@cfa.harvard.edu
Received 2018 July 20; revised 2018 September 4; accepted 2018 September 5; published 2018 October 5

Abstract

We present the initial–final mass relation (IFMR) based on the self-consistent analysis of Sirius B and 79 white dwarfs from 13 star clusters. We have also acquired additional signal on eight white dwarfs previously analyzed in the NGC 2099 cluster field, four of which are consistent with membership. These re-observed white dwarfs have masses ranging from 0.72 to 0.97 $M_{\odot}$, with initial masses from 3.0 to 3.65 $M_{\odot}$, where the IFMR has an important change in slope that these new data help to observationally confirm. In total, this directly measured IFMR has small scatter ($\sigma = 0.06\,M_{\odot}$) and spans from progenitors of 0.85 to 7.5 $M_{\odot}$. Applying two different stellar evolutionary models to infer two different sets of white dwarf progenitor masses shows that, when the same model is also used to derive the cluster ages, the resulting IFMR has weak sensitivity to the adopted model at all but the highest initial masses (>5.5 $M_{\odot}$). The nonlinearity of the IFMR is also clearly observed with moderate slopes at lower masses (0.08 $M_{\rm final}/M_{\rm initial}$) and higher masses (0.11 $M_{\rm final}/M_{\rm initial}$) that are broken up by a steep slope (0.19 $M_{\rm final}/M_{\rm initial}$) between progenitors from 2.85 to 3.6 $M_{\odot}$. This IFMR shows total stellar mass loss ranges from 33% of $M_{\rm initial}$ at 0.83 $M_{\odot}$ to 83% of $M_{\rm initial}$ at 7.5 $M_{\odot}$. Testing this total mass loss for dependence on progenitor metallicity, however, finds no detectable sensitivity across the moderate range of $-0.15 < [{\rm Fe/H}] < +0.15$.

Key words: globular clusters: individual (M4) – open clusters and associations: general – stars: evolution – stars: mass-loss – white dwarfs

1. Introduction

Stellar evolution remains a complex and difficult process to model. The final stages are the most challenging, where evolution becomes highly sensitive to convection, overshoot, dredge-up, mass loss, and nuclear reaction rates (e.g., see Marigo & Girardi 2007; Doherty et al. 2015; Choi et al. 2016). The analysis of white dwarfs, however, can provide a powerful tool to help constrain these processes (e.g., Kalirai et al. 2014). During the thermally pulsing asymptotic giant phase (hereafter TP-AGB), these stars will go through multiple pulses that expel their outer shells and eventually expose their hot central core, which becomes a white dwarf. The spectroscopic analysis of white dwarfs provides both their mass and cooling age, which is the time since it has left the tip of the AGB. For white dwarfs that are members of star clusters, the comparison of a white dwarf's cooling age to its cluster's age provides the necessary information to infer the initial mass (hereafter $M_{\rm initial}$) of its progenitor. The relation of a white dwarf's mass to its progenitor's mass is called the initial–final mass relation (hereafter the IFMR).

Significant progress has been made in the IFMR, but it has been a slow process across the past 40 years (e.g., see Weidemann 1977, 2000). The challenge of photometrically and spectroscopically characterizing these faint targets in a broad range of clusters led to a sparse IFMR with many gaps in the data, most importantly at the higher masses where white dwarfs are both rare and even fainter. To limit the relation further, there remained significant scatter. Within the past 10 years, the increasing availability of both widefield imagers and spectrographs on large telescopes has led to a significantly increased number of known white dwarfs in star clusters. This includes the work of Kalirai et al. (2005, 2008, 2009), Williams et al. (2009), Casewell et al. (2009), Dobbie et al. (2009, 2012), Cummings et al. (2015, 2016a, 2016b, hereafter Papers I, II, and III, respectively), and Raddi et al. (2016).

For many years, however, the large observed scatter in the relation left many questions about its cause. Several possibilities were considered: (1) that there are large stochastic (or environmentally dependent) variations in mass-loss rates for stars at the same $M_{\rm initial}$; (2) that mass loss and core evolution have more significant dependence on metallicity than predicted; (3) that systematics between the analysis techniques of the open clusters and of the white dwarfs artificially created this scatter. Paper II focused on minimizing the systematics resulting from differences in the white dwarf data reduction, and adopted atmospheric and cooling models, spectroscopic fitting techniques, and cluster parameters. In comparison to the IFMRs of Catalán et al. (2008b), Salaris et al. (2009), and Kalirai et al. (2008), this decreased the observed scatter of the IFMR by ∼50%.

In Paper II, however, systematic issues remained with respect to the stellar evolutionary model adopted. Two IFMRs were presented based on different stellar evolutionary models, the Yale–Yonsei isochrones (Yi et al. 2001; hereafter Y^2 isochrones) and the PARSEC isochrones (Bressan et al. 2012) version 1.2S.[6] The ages of each young cluster these white dwarfs are members of were measured with both model isochrones, but due to the Y^2 isochrones not considering

* Based on observations with the W.M. Keck Observatory, which is operated as a scientific partnership among the California Institute of Technology, the University of California, and NASA, was made possible by the generous financial support of the W.M. Keck Foundation.

[6] Available at http://stev.oapd.inaf.it/cgi-bin/cmd.

evolution after the red giant branch (hereafter RGB), in both cases the PARSEC isochrones were used to infer $M_{\rm initial}$ of the progenitors from the calculated evolutionary lifetimes. Important differences resulted in these IFMRs; for example, the Y^2-based IFMR was linear while the PARSEC-based IFMR had a clear change in slope at $M_{\rm initial} \sim 4\,M_{\odot}$.

Cummings (2017) applied these two IFMRs to test mass-loss rates and core-mass growth during the TP-AGB. This showed that the Y^2-based IFMR gave unrealistic core-mass growths for TP-AGB stars with higher $M_{\rm initial}$ ($>5\,M_{\odot}$). This likely resulted more from the inability to self-consistently infer $M_{\rm initial}$ with Y^2 models, rather than any significant limitations in Y^2-based cluster ages. Because of this limitation we will not further consider the Y^2-based IFMR in this paper.

More recently, other methods to study the IFMR have been developed. These include studying wide double-degenerate binaries (Finley & Koester 1997; Andrews et al. 2015), which can be assumed to be coeval and to have not interacted. These can constrain stellar evolution relatively, but the total age of the system cannot be derived to reliably put the analysis on a standard scale. This method also must assume the progenitor's metallicity to analyze its evolutionary timescale. Wide white dwarf main sequence binaries have also been used (Catalán et al. 2008a; Zhao et al. 2012), but these are limited in number, typically of low mass, and ages derived from a single main sequence companion have errors far larger than those of star clusters. *Gaia* DR2 data (Gaia Collaboration et al. 2016, 2018b) of white dwarfs have also been used (El-Badry et al. 2018), which provide a massive photometric sample. This photometry, however, is unable to identify a white dwarf's atmospheric make-up, which plays an important role in its photometric-based parameters, mass–radius relation, and cooling rate. Therefore, the analysis is limited to white dwarfs with previous spectroscopic identification, which introduces important selection biases (see Tremblay et al. 2016). The effects of progenitor metallicity also cannot be taken into account. Lastly, the higher-mass IFMR derived through this method is very sensitive to the adopted initial mass function.

In this paper we present new advancements of the IFMR. (1) We present new observations that increase the signal-to-noise ratio (S/N) on a subset of NGC 2099 (M37) white dwarfs that are valuable in defining the IFMR ranging from $M_{\rm initial}$ of 3 to 3.65 $M_{\odot}$. (2) We update the young cluster parameters based on the detailed cluster analysis in Cummings & Kalirai (2018). (3) We apply updated analysis techniques and models to the white dwarfs from Paper I in NGC 2099, Hyades, and Praesepe. (4) We expand this self-consistent IFMR analysis to include the sample of known lower-mass white dwarfs from NGC 6819, NGC 7789 (Kalirai et al. 2009), and NGC 6121 (M4; Kalirai et al. 2009). (5) In addition to the semi-empirical IFMR adopting PARSEC isochrones, we derive an IFMR based on stellar models and isochrones from the MIST isochrones (Choi et al. 2016; Dotter 2016), which are based on the Modules for Experiments in Stellar Astrophysics (MESA; Paxton et al. 2011, 2013, 2015). This tests the sensitivity of the semi-empirical IFMR to the adopted evolutionary model. (6) We apply the IFMR to measure total integrated mass loss and its dependence on $M_{\rm initial}$, and we test its sensitivity to metallicity over a moderate range.

The structure of the paper is as follows: in Section 2 we discuss the new spectroscopic observations of white dwarfs in NGC 2099, the use of publicly available data, and the adopted methods of data reduction. In Section 3 we discuss the adopted white dwarf atmospheric and cooling models and analysis techniques. In Section 4 we discuss the updated photometric analysis of the six intermediate-age and older star clusters and Sirius B using the PARSEC and MIST isochrones. In Section 5 we re-analyze the white dwarf memberships of the NGC 7789, NGC 6819, and NGC 6121 candidates. In Section 6 we discuss the complete IFMR and its characteristics. We additionally discuss what effects adopting the MIST model versus the PARSEC model have on the IFMR. We finally discuss total integrated mass loss and its sensitivity to metallicity. In Section 7 we summarize the work and draw conclusions.

2. Observations and Reductions

We have analyzed Sirius B and 79 white dwarf members across 13 star clusters, which range from cluster ages of 125 Myr to 12 Gyr.

For the low-mass IFMR, we have analyzed white dwarfs in the older open clusters NGC 6819 and NGC 7789 (Kalirai et al. 2008) and in the globular cluster NGC 6121 (Kalirai et al. 2009). White dwarfs in the old and metal-rich open cluster NGC 6791 have also been previously identified (Kalirai et al. 2007), but they will not be analyzed here because they are consistent with helium-core white dwarfs, which have likely undergone distinct evolution from carbon (C) and O-core and ONe-core white dwarfs (e.g., Miglio et al. 2012; Williams et al. 2018). The spectroscopic observations of these lower-mass white dwarfs were similarly taken with Keck I LRIS for NGC 6819 and NGC 7789 (with the 600/4000 grism in 2005 July 29 and 30), and NGC 6121 (with the 400/3400 grism on multiple half-nights in 2005 June, 2007 April and July, and 2008 April). We similarly re-analyzed these original observations using the same XIDL pipeline. These pipeline-processed spectra showed strong consistency with the original processed spectra from the Kalirai et al. publications, however, so we continued the analysis with the original processed spectra.

Presented first in Kalirai et al. (2005) and Papers I, II, and III, we observed three sets of intermediate-mass (0.7–1.0 $M_{\odot}$) white dwarfs in NGC 2099 using Keck I LRIS (Oke et al. 1995) and the 600/4000 and 400/3400 grisms, providing a resolution of 4 Å and 6.5 Å, respectively. Throughout this work with NGC 2099, however, the S/N of the faintest (highest mass) white dwarfs in the first observed sample (from 2002 December 04; Kalirai et al. 2005; Paper I) remained limited. These white dwarfs have masses from 0.72 to 0.97 $M_{\odot}$, which helps define the relation at $M_{\rm initial}$ of ~3 to 4 $M_{\odot}$. This is where second dredge-up begins, affecting core masses in AGB stars and hence their final white dwarf masses.

Keck I LRIS with the 600/4000 grism was used again on 2016 November 29 to re-observe eight white dwarfs in the field NGC 2099. Weather conditions were only fair, which limited the amount of light received, but they still provided an important addition to the previous observations. As in Papers I, II, and III, we again reduced and flux calibrated the LRIS observations using the IDL-based XIDL pipeline.[7] We subsequently co-added these new observations to the original observations of these white dwarfs from 2002 presented in Kalirai et al. (2005) and Paper I.

Praesepe is a well-studied cluster that we have included in all three previous papers of our series. Casewell et al. (2009)

[7] Available at http://www.ucolick.org/~xavier/IDL/.

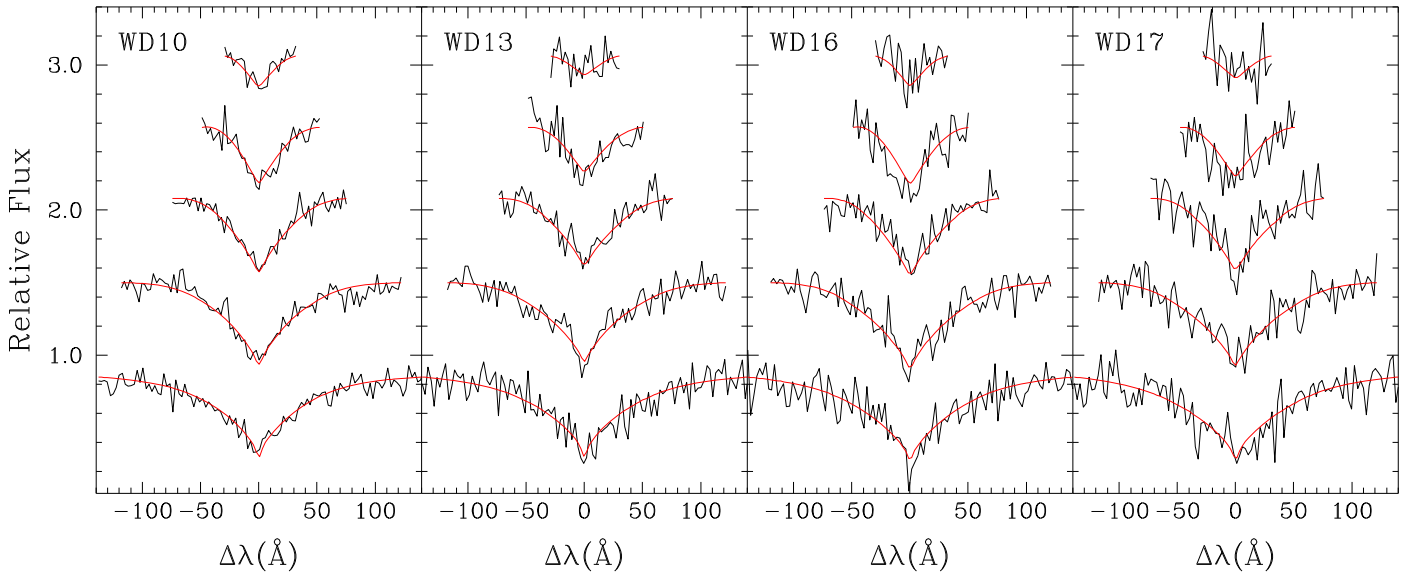

Figure 1. Balmer line fits for the co-added spectra of the four re-observed white dwarfs consistent with membership in NGC 2099, which are binned for display purposes. Hβ, Hγ, Hδ, Hϵ, and H8 are shown from bottom to top.

observed seven Praesepe white dwarfs at high signal-to-noise with VLT/UVES spectroscopy. Previously, we used the Praesepe white dwarf parameters presented for these data from Kalirai et al. (2014), but here we acquired these pipeline-processed Praesepe data directly from the ESO Archive. These spectra were coadded and flux corrected by consistent observations of the flux standard WD0000–345.

Finally, we analyzed the white dwarfs from the intermediate-age NGC 1039 (Rubin et al. 2008). Its three high-mass and three low-mass white dwarfs were found to have luminosities consistent with membership, but only the three high-mass white dwarfs had proper motions consistent with membership (Dobbie et al. 2009). These NGC 1039 white dwarfs were similarly observed with Keck I LRIS and the 400/3400 grism. We acquired the data for these three high-mass white dwarfs from the Keck archive and similarly analyzed them using the XIDL pipeline.

3. White Dwarf Atmosphere Models and Cooling Models

The white dwarf atmospheric analysis in our paper series has and continues to use the 1D models of Tremblay et al. (2011) with the Stark broadening profiles of Tremblay & Bergeron (2009) and the automated spectral fitting techniques of Bergeron et al. (1992). Simultaneously fitting the five pressure-sensitive Balmer features from Hβ to H8 from each white dwarf measures their $T_{\rm eff}$ and log g based solely on spectroscopic analysis. We note that the entire sample of white dwarfs in this paper consists of higher-temperature DAs ($T_{\rm eff} \geqslant 14{,}500$ K) where there is negligible to no convection occurring. Using the 3D models including convection from Tremblay et al. (2013) would not affect the results.

For the white dwarf parameters, we also consider the errors based on the noise, the quality of the Balmer line matches, and the external errors resulting from the data calibration. These external errors are estimated to be 1.2% in $T_{\rm eff}$ and 0.038 dex in log g (Liebert et al. 2005). The combination in quadrature of both internal and external errors provides the total estimated uncertainties.

In Figure 1 we show the updated spectroscopic analysis of the four re-observed NGC 2099 white dwarfs consistent with membership. These spectra have been co-added to the earlier observations. The other four re-observed NGC 2099 white dwarfs are not shown because they either remained inconsistent with membership or still gave errors beyond the error cuts applied to this sample (see Paper I for more information on these).

We similarly analyzed the ESO archive pipeline processed spectra of the Praesepe white dwarfs and the Keck I LRIS spectra of the white dwarfs from NGC 1039, NGC 6121, NGC 6819, and NGC 7789. The Praesepe spectra were originally analyzed in Casewell et al. (2009) with the atmospheric models of TLUSTY, v200 (Hubeny 1988; Hubeny & Lanz 1995) and the spectral synthesis code SYNSPEC v48 (Hubeny et al. 2001). All of these remaining cluster white dwarf spectra were analyzed in their original publications with the fitting techniques from Bergeron et al. (1992), as used here, but also with the atmospheric models from that work. See Table 1 for the updated log g and $T_{\rm eff}$.

Application of these derived log g and $T_{\rm eff}$ to white dwarf cooling models provides the mass, cooling age, luminosity, and intrinsic colors. Our paper series adopted the CO-core models with thick H envelopes from Fontaine et al. (2001) for all white dwarfs with masses of 1.1 $M_{\odot}$ and below. For higher-mass white dwarfs, as in Paper III, we adopt the ONe-core models of Althaus et al. (2007). Because these ONe-core white dwarfs only have cooling ages from ∼50 to 250 Myr, the recently updated ONe-core models from Camisassa et al. (2018) give consistent results.

4. Photometric Analysis of Star Clusters

Deriving an IFMR requires linking the white dwarf properties to their progenitor stars. This is performed through analysis of the host clusters, which is just as important as the white dwarf analysis for two reasons: first, a white dwarf's cluster membership and single-star status can be tested by comparing its intrinsic and observed characteristics relative to the cluster's

Table 1
Re-analyzed White Dwarf and Progenitor Parameters

ID	$T_{\rm eff}$ (K)	log g	$M_{\rm f}$ ($M_\odot$)	$t_{\rm cool}$ (Myr)	PARSEC $M_{\rm i}$ ($M_\odot$)	MIST $M_{\rm i}$ ($M_\odot$)	S/N[a]
Reobserved NGC 2099 White Dwarf Members							
NGC 2099-WD10	19250 ± 500	8.160 ± 0.084	0.717 ± 0.049	115^{+23}_{-21}	$2.99^{+0.05}_{-0.04}$	$3.03^{+0.06}_{-0.05}$	43
NGC 2099-WD13	20250 ± 850	8.526 ± 0.126	0.949 ± 0.078	199^{+58}_{-47}	$3.19^{+0.19}_{-0.12}$	$3.25^{+0.20}_{-0.13}$	30
NGC 2099-WD16	17150 ± 850	8.334 ± 0.144	0.823 ± 0.092	230^{+75}_{-59}	$3.29^{+0.29}_{-0.17}$	$3.35^{+0.31}_{-0.18}$	24
NGC 2099-WD17	18000 ± 950	8.571 ± 0.154	0.974 ± 0.092	302^{+102}_{-82}	$3.57^{+0.64}_{-0.31}$	$3.64^{+0.70}_{-0.33}$	25
Rederived Praesepe, NGC 7789, NGC 6819, and NGC 6121 Members							
Prae WD0833+194	14500 ± 300	8.325 ± 0.042	0.813 ± 0.027	364^{+33}_{-30}	$3.40^{+0.12}_{-0.10}$	$3.51^{+0.12}_{-0.10}$	173
Prae WD0836+199	14900 ± 300	8.351 ± 0.043	0.830 ± 0.028	352^{+34}_{-31}	$3.36^{+0.12}_{-0.10}$	$3.41^{+0.12}_{-0.10}$	130
Prae WD0837+185	14750 ± 350	8.413 ± 0.046	0.870 ± 0.029	402^{+42}_{-39}	$3.54^{+0.19}_{-0.14}$	$3.65^{+0.19}_{-0.14}$	140
Prae WD0837+199	17200 ± 200	8.230 ± 0.040	0.757 ± 0.025	190^{+16}_{-15}	$2.96^{+0.03}_{-0.03}$	$3.02^{+0.03}_{-0.03}$	216
Prae WD0840+190	14800 ± 400	8.452 ± 0.047	0.895 ± 0.030	425^{+48}_{-44}	$3.64^{+0.25}_{-0.18}$	$3.76^{+0.26}_{-0.17}$	106
Prae WD0840+200	16050 ± 200	8.226 ± 0.042	0.752 ± 0.027	233^{+19}_{-18}	$3.05^{+0.04}_{-0.04}$	$3.12^{+0.05}_{-0.04}$	134
Prae WD0843+184	14850 ± 300	8.456 ± 0.043	0.898 ± 0.028	423^{+38}_{-41}	$3.63^{+0.19}_{-0.17}$	$3.75^{+0.20}_{-0.16}$	173
NGC 6121 WD00	20900 ± 500	7.771 ± 0.076	0.507 ± 0.036	35^{+6}_{-4}	$0.87^{+0.01}_{-0.01}$	$0.83^{+0.01}_{-0.01}$	49
NGC 6121 WD04	25450 ± 550	7.776 ± 0.074	0.522 ± 0.034	16^{+1}_{-1}	$0.87^{+0.01}_{-0.01}$	$0.83^{+0.01}_{-0.01}$	64
NGC 6121 WD05	28850 ± 500	7.767 ± 0.072	0.527 ± 0.032	$10^{+0.6}_{-0.6}$	$0.87^{+0.01}_{-0.01}$	$0.83^{+0.01}_{-0.01}$	78
NGC 6121 WD06	26350 ± 500	7.903 ± 0.069	0.587 ± 0.035	15^{+3}_{-1}	$0.87^{+0.01}_{-0.01}$	$0.83^{+0.01}_{-0.01}$	56
NGC 6121 WD15	24600 ± 600	7.887 ± 0.081	0.574 ± 0.041	19^{+5}_{-2}	$0.87^{+0.01}_{-0.01}$	$0.83^{+0.01}_{-0.01}$	47
NGC 6121 WD20	21050 ± 550	7.792 ± 0.084	0.517 ± 0.040	34^{+7}_{-4}	$0.87^{+0.01}_{-0.01}$	$0.83^{+0.01}_{-0.01}$	44
NGC 6121 WD24	26250 ± 500	7.789 ± 0.069	0.530 ± 0.032	$14^{+1}_{-0.9}$	$0.87^{+0.01}_{-0.01}$	$0.83^{+0.01}_{-0.01}$	64
NGC 6819-6	21700 ± 350	7.944 ± 0.051	0.597 ± 0.028	40^{+7}_{-5}	$1.61^{+0.01}_{-0.01}$	$1.58^{+0.01}_{-0.01}$	97
NGC 7789-5	31700 ± 450	8.116 ± 0.061	0.714 ± 0.036	$8^{+0.8}_{-1}$	$1.90^{+0.01}_{-0.01}$	$1.79^{+0.01}_{-0.01}$	91
NGC 7789-8	24800 ± 550	8.114 ± 0.074	0.700 ± 0.044	32^{+10}_{-8}	$1.91^{+0.01}_{-0.01}$	$1.81^{+0.01}_{-0.01}$	58
NGC 7789-11	20500 ± 650	8.270 ± 0.095	0.787 ± 0.060	117^{+28}_{-25}	$1.96^{+0.01}_{-0.01}$	$1.85^{+0.03}_{-0.02}$	46
NGC 7789-14	21100 ± 1000	7.987 ± 0.144	0.619 ± 0.080	52^{+28}_{-18}	$1.92^{+0.02}_{-0.01}$	$1.82^{+0.01}_{-0.01}$	24
Self-consistent Parameter Derivations for NGC 1039 White Dwarfs and Those from Papers II and III							
NGC 1039-WD15	25900 ± 500	8.58 ± 0.07	0.990 ± 0.044	103^{+19}_{-17}	$5.81^{+0.71}_{-0.46}$	$5.42^{+0.51}_{-0.36}$	66
NGC 1039-WD17	26050 ± 350	8.61 ± 0.05	1.005 ± 0.028	108^{+13}_{-12}	$5.95^{+0.47}_{-0.35}$	$5.53^{+0.34}_{-0.27}$	135
NGC 1039-WDS2	31600 ± 400	8.46 ± 0.04	0.921 ± 0.027	31^{+6}_{-4}	$4.48^{+0.07}_{-0.04}$	$4.32^{+0.06}_{-0.04}$	303
NGC 2099-WD2	22200 ± 650	8.24 ± 0.07	0.77 ± 0.045	81^{+18}_{-16}	$2.92^{+0.04}_{-0.03}$	$2.95^{+0.04}_{-0.03}$	55
NGC 2099-WD5	18100 ± 650	8.21 ± 0.01	0.74 ± 0.062	156^{+36}_{-32}	$3.08^{+0.09}_{-0.07}$	$3.13^{+0.10}_{-0.08}$	34
NGC 2099-WD6	16700 ± 750	8.44 ± 0.11	0.89 ± 0.069	299^{+73}_{-62}	$3.55^{+0.40}_{-0.24}$	$3.63^{+0.44}_{-0.26}$	32
NGC 2099-WD9	16200 ± 800	7.95 ± 0.14	0.59 ± 0.078	139^{+47}_{-38}	$3.04^{+0.12}_{-0.08}$	$3.08^{+0.13}_{-0.09}$	27
NGC 2099-WD18	24900 ± 600	8.21 ± 0.06	0.76 ± 0.036	44^{+11}_{-10}	$2.85^{+0.02}_{-0.02}$	$2.87^{+0.02}_{-0.02}$	75
NGC 2099-WD21	16900 ± 700	8.37 ± 0.11	0.85 ± 0.069	258^{+63}_{-52}	$3.39^{+0.27}_{-0.17}$	$3.45^{+0.29}_{-0.18}$	36
NGC 2099-WD24	18700 ± 700	8.29 ± 0.11	0.80 ± 0.068	163^{+40}_{-35}	$3.10^{+0.11}_{-0.08}$	$3.14^{+0.12}_{-0.09}$	42
NGC 2099-WD25	27500 ± 450	8.11 ± 0.06	0.70 ± 0.03	17^{+5}_{-3}	$2.80^{+0.01}_{-0.01}$	$2.82^{+0.01}_{-0.01}$	82
NGC 2099-WD28	22000 ± 400	8.20 ± 0.06	0.75 ± 0.03	76^{+13}_{-12}	$2.91^{+0.03}_{-0.02}$	$2.94^{+0.03}_{-0.02}$	80
NGC 2099-WD33	32900 ± 1100	9.27 ± 0.22	$1.28^{+0.05}_{-0.08}$	233^{+102}_{-118}	$3.30^{+0.43}_{-0.31}$	$3.36^{+0.46}_{-0.34}$	22
NGC 2168-LAWDS1	33500 ± 450	8.44 ± 0.06	0.911 ± 0.039	19^{+7}_{-6}	$4.39^{+0.08}_{-0.06}$	$4.35^{+0.08}_{-0.06}$	122
NGC 2168-LAWDS2	33400 ± 600	8.49 ± 0.10	0.940 ± 0.061	25^{+13}_{-10}	$4.46^{+0.16}_{-0.11}$	$4.42^{+0.16}_{-0.11}$	60
NGC 2168-LAWDS5	52700 ± 900	8.21 ± 0.06	0.801 ± 0.031	$1.0^{+0.1}_{-0.1}$	$4.19^{+0.01}_{-0.01}$	$4.16^{+0.01}_{-0.01}$	225
NGC 2168-LAWDS6	57300 ± 1000	8.05 ± 0.06	0.731 ± 0.029	$0.5^{+0.1}_{-0.1}$	$4.20^{+0.01}_{-0.01}$	$4.17^{+0.01}_{-0.01}$	250
NGC 2168-LAWDS11	19900 ± 350	8.35 ± 0.05	0.834 ± 0.035	149^{+18}_{-17}	$10.44^{+*}_{-2.67}$	$9.13^{+11.1}_{-1.75}$	90
NGC 2168-LAWDS12	34200 ± 500	8.60 ± 0.06	1.009 ± 0.037	36^{+9}_{-8}	$4.58^{+0.12}_{-0.10}$	$4.54^{+0.11}_{-0.10}$	100
NGC 2168-LAWDS14	30500 ± 450	8.57 ± 0.06	0.988 ± 0.038	54^{+11}_{-10}	$4.86^{+0.20}_{-0.16}$	$4.78^{+0.18}_{-0.14}$	98
NGC 2168-LAWDS15	30100 ± 400	8.61 ± 0.06	1.009 ± 0.032	64^{+10}_{-10}	$5.03^{+0.21}_{-0.18}$	$4.93^{+0.20}_{-0.16}$	110
NGC 2168-LAWDS22	53000 ± 1000	8.22 ± 0.06	0.807 ± 0.035	$1.0^{+0.1}_{-0.1}$	$4.20^{+0.01}_{-0.01}$	$4.17^{+0.00}_{-0.01}$	233
NGC 2168-LAWDS27	30700 ± 400	8.72 ± 0.06	1.071 ± 0.031	78^{+12}_{-11}	$5.35^{+0.30}_{-0.24}$	$5.24^{+0.31}_{-0.24}$	125
NGC 2168-LAWDS29	33500 ± 450	8.56 ± 0.06	0.984 ± 0.034	34^{+8}_{-8}	$4.56^{+0.11}_{-0.10}$	$4.52^{+0.10}_{-0.09}$	94
NGC 2168-LAWDS30	29700 ± 500	8.39 ± 0.08	0.878 ± 0.048	33^{+12}_{-10}	$4.55^{+0.16}_{-0.12}$	$4.51^{+0.15}_{-0.12}$	60
NGC 2287-2	25900 ± 350	8.45 ± 0.05	0.909 ± 0.028	76^{+10}_{-9}	$4.82^{+0.17}_{-0.13}$	$4.83^{+0.17}_{-0.14}$	164
NGC 2287-4	26500 ± 350	8.71 ± 0.05	1.065 ± 0.027	127^{+14}_{-13}	$6.02^{+0.65}_{-0.41}$	$6.06^{+0.64}_{-0.43}$	144
NGC 2287-5	25600 ± 350	8.44 ± 0.04	0.901 ± 0.028	77^{+10}_{-9}	$4.85^{+0.17}_{-0.14}$	$4.86^{+0.18}_{-0.14}$	189

Table 1
(Continued)

ID	$T_{\rm eff}$ (K)	log g	$M_{\rm f}$ ($M_\odot$)	$t_{\rm cool}$ (Myr)	PARSEC $M_{\rm i}$ ($M_\odot$)	MIST $M_{\rm i}$ ($M_\odot$)	S/N[a]
NGC 2323-WD10	52800 ± 1350	8.68 ± 0.09	1.068 ± 0.045	$1.6^{+1.2}_{-0.6}$	$5.06^{+0.02}_{-0.01}$	$4.90^{+0.02}_{-0.01}$	87
NGC 2323-WD11	54100 ± 1000	8.69 ± 0.07	1.075 ± 0.032	$1.3^{+0.6}_{-0.4}$	$5.05^{+0.01}_{-0.01}$	$4.89^{+0.01}_{-0.01}$	126
NGC 2516-1	30100 ± 350	8.47 ± 0.04	0.925 ± 0.027	42^{+7}_{-7}	$4.62^{+0.11}_{-0.09}$	$4.29^{+0.08}_{-0.06}$	270
NGC 2516-2	35500 ± 550	8.55 ± 0.07	0.981 ± 0.040	24^{+8}_{-7}	$4.83^{+0.11}_{-0.09}$	$4.44^{+0.08}_{-0.06}$	83
NGC 2516-3	29100 ± 350	8.46 ± 0.04	0.918 ± 0.027	48^{+8}_{-7}	$4.89^{+0.12}_{-0.11}$	$4.49^{+0.08}_{-0.08}$	207
NGC 2516-5	32200 ± 400	8.54 ± 0.05	0.970 ± 0.027	38^{+7}_{-6}	$4.98^{+0.15}_{-0.12}$	$4.55^{+0.10}_{-0.08}$	213
NGC 3532-1	23100 ± 300	8.52 ± 0.04	0.950 ± 0.026	131^{+13}_{-12}	$3.95^{+0.09}_{-0.08}$	$3.86^{+0.08}_{-0.07}$	210
NGC 3532-5	27700 ± 350	8.28 ± 0.05	0.804 ± 0.028	31^{+7}_{-6}	$3.44^{+0.03}_{-0.02}$	$3.39^{+0.03}_{-0.02}$	232
NGC 3532-9	31900 ± 400	8.18 ± 0.04	0.752 ± 0.026	9.3^{+2}_{-1}	$3.36^{+0.01}_{-0.01}$	$3.31^{+0.01}_{-0.01}$	236
NGC 3532-10	26300 ± 350	8.34 ± 0.04	0.838 ± 0.027	51^{+8}_{-8}	$3.52^{+0.03}_{-0.03}$	$3.46^{+0.03}_{-0.03}$	234
NGC 3532-J1106-584	20200 ± 300	8.52 ± 0.05	0.945 ± 0.029	197^{+20}_{-18}	$4.54^{+0.27}_{-0.20}$	$4.38^{+0.23}_{-0.17}$	149
NGC 3532-J1106-590	21100 ± 350	8.48 ± 0.05	0.922 ± 0.031	163^{+18}_{-17}	$4.20^{+0.17}_{-0.14}$	$4.07^{+0.15}_{-0.12}$	124
NGC 3532-J1107-584	20700 ± 300	8.59 ± 0.05	0.990 ± 0.028	211^{+21}_{-20}	$4.73^{+0.34}_{-0.25}$	$4.54^{+0.29}_{-0.22}$	193
VPHASJ1103-5837	23900 ± 450	8.87 ± 0.06	1.11 ± 0.03	223^{+40}_{-30}	$4.91^{+0.90}_{-0.41}$	$4.69^{+0.73}_{-0.35}$	⋯
Sirius B	26000 ± 400	8.57 ± 0.04	0.982 ± 0.024	99^{+11}_{-10}	$4.58^{+0.14}_{-0.12}$	$4.88^{+0.18}_{-0.14}$	⋯
Pleiades-LB 1497	32700 ± 500	8.67 ± 0.05	1.046 ± 0.028	54^{+9}_{-8}	$6.61^{+0.51}_{-0.34}$	$5.86^{+0.31}_{-0.23}$	187
GD50	42700 ± 800	9.20 ± 0.07	1.26 ± 0.02	76^{+17}_{-11}	$8.21^{+2.86}_{-0.99}$	$6.74^{+1.21}_{-0.52}$	⋯
PG 0136+251	41400 ± 800	9.03 ± 0.07	1.20 ± 0.03	52^{+14}_{-12}	$6.49^{+0.80}_{-0.45}$	$5.78^{+0.48}_{-0.33}$	⋯
Hyades HS0400+1451	14620 ± 60	8.25 ± 0.01	0.765 ± 0.006	316^{+10}_{-9}	$3.26^{+0.02}_{-0.02}$	$3.36^{+0.02}_{-0.02}$	⋯
Hyades WD0348+339	14820 ± 350	8.31 ± 0.05	0.804 ± 0.032	331^{+40}_{-36}	$3.32^{+0.12}_{-0.10}$	$3.42^{+0.13}_{-0.10}$	⋯
Hyades WD0352+096	14670 ± 380	8.30 ± 0.05	0.797 ± 0.032	339^{+41}_{-37}	$3.33^{+0.13}_{-0.10}$	$3.44^{+0.13}_{-0.11}$	⋯
Hyades WD0406+169	15810 ± 290	8.38 ± 0.05	0.850 ± 0.032	316^{+31}_{-28}	$3.26^{+0.10}_{-0.08}$	$3.36^{+0.10}_{-0.09}$	⋯
Hyades WD0421+162	20010 ± 320	8.13 ± 0.05	0.700 ± 0.03	93^{+14}_{-12}	$2.80^{+0.02}_{-0.02}$	$2.84^{+0.02}_{-0.02}$	⋯
Hyades WD0425+168	25130 ± 380	8.12 ± 0.05	0.704 ± 0.029	31^{+6}_{-5}	$2.71^{+0.01}_{-0.01}$	$2.74^{+0.01}_{-0.01}$	⋯
Hyades WD0431+126	21890 ± 350	8.11 ± 0.05	0.691 ± 0.03	60^{+11}_{-9}	$2.75^{+0.01}_{-0.01}$	$2.79^{+0.02}_{-0.02}$	⋯
Hyades WD0437+138	15120 ± 360	8.25 ± 0.09	0.766 ± 0.057	295^{+52}_{-44}	$3.18^{+0.14}_{-0.10}$	$3.28^{+0.15}_{-0.12}$	⋯
Hyades WD0438+108	27540 ± 400	8.15 ± 0.05	0.726 ± 0.03	20^{+5}_{-4}	$2.70^{+0.01}_{-0.00}$	$2.73^{+0.01}_{-0.01}$	⋯
Hyades WD0625+415	17610 ± 280	8.07 ± 0.05	0.659 ± 0.03	132^{+16}_{-14}	$2.86^{+0.03}_{-0.02}$	$2.91^{+0.03}_{-0.03}$	⋯
Hyades WD0637+477	14650 ± 590	8.30 ± 0.06	0.797 ± 0.039	339^{+50}_{-44}	$3.34^{+0.19}_{-0.14}$	$3.44^{+0.19}_{-0.15}$	⋯

Note.
[a] Presented S/Ns are per resolution element, which for a majority of these data is ∼6 Å. For white dwarfs observed at higher resolutions we similarly scale the presented S/Ns to per 6 Å element to represent data quality on a uniform scale. Note that in this table and in Equations (1) through (6), $M_{\rm final}$ and $M_{\rm initial}$ have been abbreviated to $M_{\rm f}$ and $M_{\rm i}$, respectively.

reddening and distance modulus.[8] Poor membership determinations increase contamination from field white dwarfs, which increases the scatter and number of outliers in the IMFR. Many double-degenerate cluster members will also be removed because they will appear too bright, which is helpful because binary interactions may have affected their evolution. Second, the cluster's age is needed compare to the white dwarf member's cooling age to determine the evolutionary lifetime for the progenitor of that white dwarf.

The final step in deriving the IFMR is to apply an evolutionary model to infer $M_{\rm initial}$ of a star with that evolutionary lifetime. Photometric main sequence and turnoff analysis are ideal because a self-consistent model can be used to derive distance modulus, cluster age, and $M_{\rm initial}$ of a star that completes its evolution at a time based on this cluster age. Cummings & Kalirai (2018) further developed the color–color techniques successfully applied to the six young clusters in Paper II. This provides a self-consistent cluster reddening and identifies turnoff stars unaffected by differential reddening and various peculiarities that would affect young cluster main sequence turnoff analysis. Here we take the updated cluster parameters directly from Cummings & Kalirai (2018).

For the case of the ultramassive white dwarf GD50, based on the work of Dobbie et al. (2006), we have adopted it as coeval with the Pleiades. However, Gagné et al. (2018) have argued, based on *Gaia* DR2 results, that it is a part of the AB Doradus moving group. For our analysis, though, this distinction is not important because the ages of the Pleiades and AB Doradus are consistent. Luhman et al. (2005) and Ortega et al. (2007) also argue that they are coeval and related groups.

In the following subsections we will analyze the parameters of the Sirius system and the intermediate-age and older clusters. The young cluster color–color analysis techniques from Cummings & Kalirai (2018) are not applicable here because they require the special characteristics of higher-mass turnoff stars with $(B-V)_0 < 0.0$. However, here we will apply similar color–magnitude age fitting techniques using non-rotating PARSEC and MIST isochrones for deriving cluster

[8] See Papers I, II, III and references therein for membership analyses for all intermediate- and high-mass white dwarfs discussed here, although we will update memberships for the NGC 7789, NGC 6819, and NGC 6121 white dwarfs in Section 4.

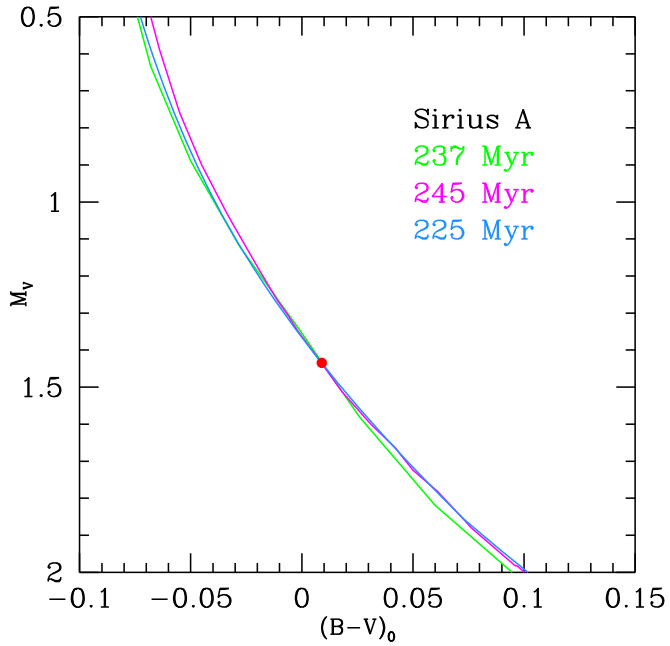

Figure 2. Color–magnitude diagram analysis of Sirius A using the Y^2 (green), PARSEC (magenta), and MIST (blue) isochrones. The measured ages are given.

parameters and the parameters of the Sirius system. Cummings & Kalirai (2018) found that turnoff ages using non-rotating PARSEC and MIST isochrones for clusters >100 Myr were consistent with lithium depletion boundary age methods.

4.1. Sirius System

The Sirius system has well determined ages (e.g., Liebert et al. 2005; Bond et al. 2017), but one of this paper's primary goals is self-consistency of age analysis using the same techniques and isochrones. Direct color–magnitude analysis of Sirius A is more limited than similar cluster turnoff analysis which covers multiple stars across a broad range of masses. Additionally, at Sirius A's age it would be a star just below the turnoff, so its color–magnitude is less sensitive to age compared to stars at the top of the turnoff. However, the well-studied Sirius A provides an accurate single photometric data point. For example, in addition to their age analysis using luminosity, $T_{\rm eff}$, and radius, Bond et al. (2017) found that a Y^2 isochrone of appropriate metallicity ([Fe/H] = −0.07; $Z = 0.0156$) measures the absolute magnitude and $B - V$ of Sirius A with an appropriate age of 220 Myr.

Here we take the photometric color and distance of Sirius A from the *Hipparcos* analysis of van Leeuwen (2007) confirmed by the recent *Gaia* DR2) and the apparent magnitude from Ducati et al. (2001). In Figure 2, Sirius A is matched to a Y^2 isochrone of $Z = 0.0156$ at 237 Myr, which is in remarkable agreement with the ages derived in Liebert et al. (2005; 237.5 ± 12.5 Myr) and Bond et al. (2017) 242 ± 15 Myr).

This provides an ideal reference to compare a Y^2 age to those derived from the PARSEC and MIST isochrones. Due to the distance of Sirius being accurately determined, when matching the PARSEC and MIST isochrones we cannot adopt the same [Fe/H] = −0.07 because each isochrone has a differing $Z_\odot$. Doing so causes luminosity shifts inconsistent with observations. Therefore, we instead adopt a uniform Z of 0.0156 for all models, which is consistent with [Fe/H] = −0.07 on the Y^2 scale. This finds a PARSEC age of 245 Myr and a MIST age of 225 Myr. These are again consistent with the luminosity, $T_{\rm eff}$, and radius analyses, but illustrate differences between the isochronal ages that are important to account for in the derivation of Sirius B's progenitor mass. Lastly, we note that it is appropriate to base the Sirius A age on these non-rotating models because it is a slow rotator at $v \sin i = 16.7$ km s^{-1} (Gray 2014), which is approximately 3.5% of Sirius A's $v_{\rm crit}$.

Due to the challenges of deriving ages of main sequence stars with white dwarf companions, in particular for lower-mass main sequence stars, this is the only white dwarf considered in this paper that is not from a star cluster.

4.2. Intermediate-age and Older Clusters

We extend our study to lower-mass white dwarfs with the analysis of intermediate-age and older clusters. In Paper I we analyzed white dwarfs in NGC 2099 and compared them to those in the Hyades and Praesepe from Kalirai et al. (2014). We performed thorough cluster parameter analysis of NGC 2099 based on its previous studies and the deep Canada–France–Hawaii Telescope photometry of the cluster from Kalirai et al. (2001b). Here, we have been able to clean the color–magnitude diagram by only displaying members based on both *Gaia* DR2 parallax and proper motions. Adopting the same reddening from Paper I, in the upper-left panel of Figure 3 we show the updated PARSEC and non-rotating MIST model ages.

Cummings et al. (2017) presented a thorough analysis of the photometry and spectroscopic metallicity of both the Hyades and Praesepe, and turnoff ages were measured for these clusters with Y^2 isochrones. Each star's absolute magnitude was calculated independently based on its individual *Hipparcos* distance published in the updated *Hipparcos* results from van Leeuwen (2007). These individual distances led to a narrower Hyades main sequence, but it still was unnaturally broad. For the current analysis a higher precision in photometric age analysis is necessary, and we have adopted the secular parallaxes for individual Hyades members calculated in de Bruijne et al. (2001). In comparison to standard trigonometric parallaxes this provides more accurate relative distances for each star and a tighter photometric main sequence and turnoff in the Hyades. These secular parallaxes are also consistent with the recently released *Gaia* DR2 parallaxes, giving that re-analysis using these new distances was not needed. In the upper-center and upper-right panels of Figure 3 we fit with PARSEC and non-rotating MIST isochrones the updated absolute photometry of the Hyades and the same Praesepe photometry used in Cummings et al. (2017).

In the lower-left and lower-center panels of Figure 3 we analyze NGC 7789 and NGC 6819. Deep and consistent BV photometry is available for these first two clusters from Kalirai et al. (2008, 2001a). To analyze these two clusters as uniformly as possible, we adopt as starting points the $E(B - V)$ and spectroscopic [Fe/H] from the same research group: for NGC 6819 we adopt parameters from Anthony-Twarog et al. (2014) and Lee-Brown et al. (2015) and for NGC 7789 we adopt parameters from Twarog et al. (2012) and Rich et al. (2013). To derive these two cluster ages photometrically, we make adjustments to the distance moduli and, if necessary, make correlated adjustments to these published reddenings and [Fe/H] within their stated error ranges to match the isochrones to their turnoffs, subgiants, and giants.

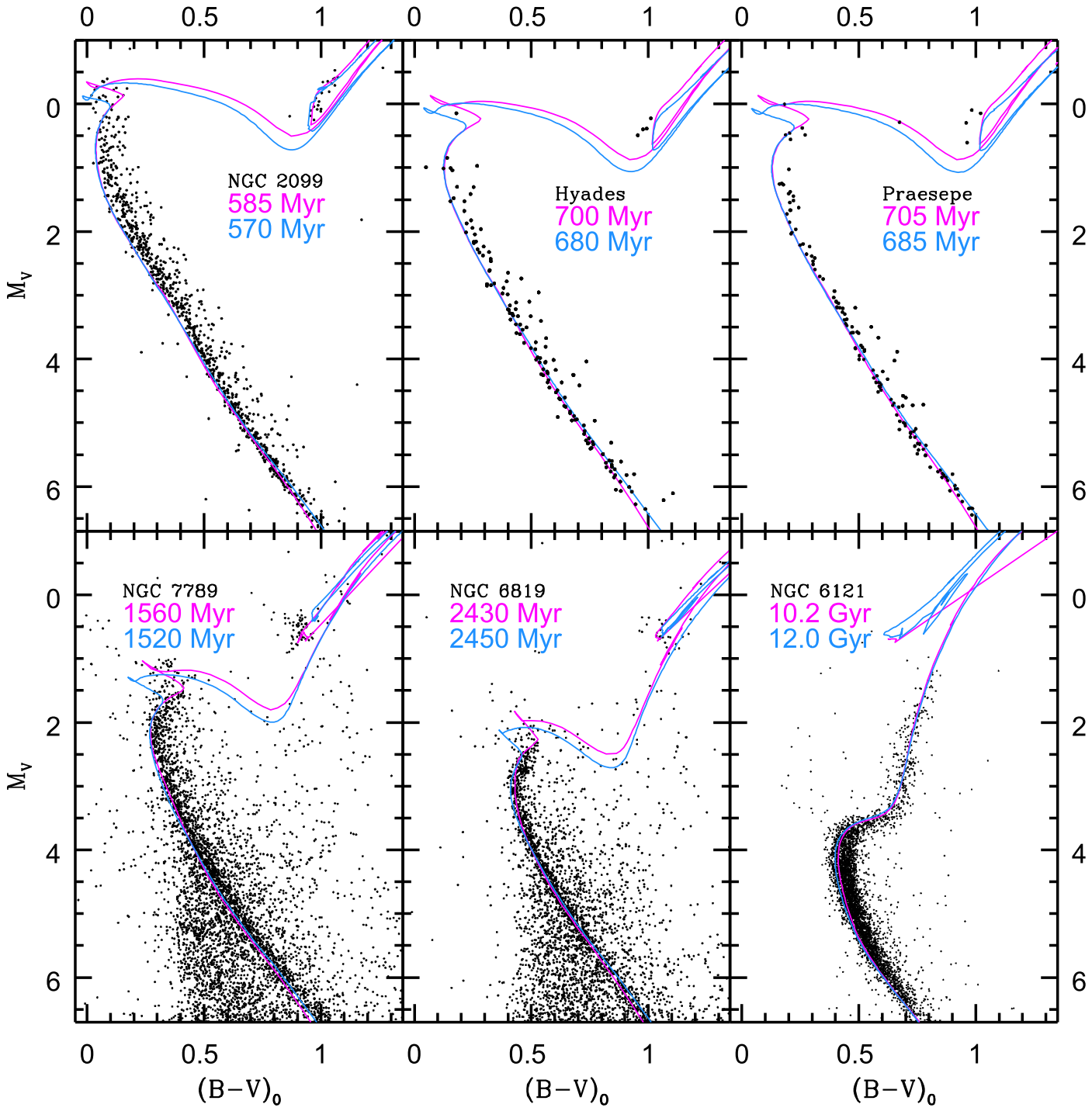

Figure 3. Color–magnitude analysis of the six older star clusters. The PARSEC isochrone ages are shown in magenta and the non-rotating MIST isochrone ages are shown in blue. See Table 2 for the photometric sources and the cluster parameters.

Finally, in the lower-right panel of Figure 3 we analyze the much older globular cluster NGC 6121. The photometry is taken from Kaluzny et al. (2013), with applied *Gaia* DR2-based membership, and the [Fe/H] of −1.1 is based on the analysis of Malavolta et al. (2014). The field of NGC 6121 has moderate differential reddening (e.g., Kaluzny et al. 2013), but we adopt a spatially independent reddening of 0.39 with only a correction based on intrinsic color. Additionally, Malavolta et al. (2014) find that the RGB sequence has a [Fe/H] ∼ 0.1 dex richer than the main sequence/subgiants. This is consistent with the theoretical effects of diffusion on Fe (see Dotter et al. 2017), but here we adopt a uniform metallicity for the cluster. The age analysis could be more thorough for NGC 6121 by accounting for these two issues, but this age is used to derive $M_{\rm initial}$ of low-mass (∼0.85 $M_{\odot}$) stars. This mass has low sensitivity to evolutionary lifetime and, unlike for higher-mass progenitors, a more thorough turnoff age analysis is not necessary.

The star cluster and Sirius system parameters are given in Table 2.

Table 2
Star Cluster Parameters

Cluster	$E(B-V)$[a]	[Fe/H]	[Fe/H] Sources	PARSEC (Myr)	MIST (Myr)	$(m-M)_0$	Phot Sources
NGC 2323	0.230 ± 0.05	0.00	⋯	115 ± 35	125 ± 35	9.86 ± 0.10	12, 13
Pleiades	0.030 ± 0.02	+0.01	3	115 ± 15	135 ± 15	5.52 ± 0.06	11
NGC 2516	0.090 ± 0.03	0.00	1	165 ± 25	195 ± 25	8.01 ± 0.12	14, 15
NGC 2168	0.240 ± 0.05	−0.143	4	175 ± 30	180 ± 30	9.52 ± 0.10	16
NGC 1039	0.100 ± 0.03	0.00	2	185 ± 25	200 ± 25	8.30 ± 0.10	17, 18
NGC 2287	0.030 ± 0.02	−0.11	2	200 ± 25	200 ± 25	9.11 ± 0.08	19, 20
Sirius	0.00	$Z = 0.0156$	5	245 ± 30	225 ± 30	−2.89 ± 0.01	21, 22
NGC 3532	0.030 ± 0.02	0.00	2	345 ± 30	360 ± 30	8.28 ± 0.14	23, 24
NGC 2099	0.225 ± 0.03	0.00	6	585 ± 50	570 ± 50	10.84 ± 0.10	25
Hyades	0.00	+0.15	7	700 ± 25	705 ± 25	3.33 ± 0.05	26
Praesepe	0.00	+0.15	7	705 ± 25	685 ± 25	6.29 ± 0.05	26
NGC 7789	0.280 ± 0.03	−0.20	8	1560 ± 100	1520 ± 100	11.66 ± 0.10	27
NGC 6819	0.165 ± 0.03	−0.04	9	2430 ± 150	2450 ± 150	11.94 ± 0.10	27
NGC 6121	0.390 ± 0.05	−1.10	10	10200 ± 1000	12000 ± 1000	11.82 ± 0.10	28

Note.
[a] We have adopted the color-dependent reddening relation of Fernie (1963) and give the derived reddenings at a color of $(B-V)_0 = 0$. We calculate true distance moduli based on extinctions of $A_V = 3.1 \times E(B-V)$. The spectroscopic sources are (1) Cummings (2011), (2) Netopil et al. (2016), (3) Schuler et al. (2010), (4) Steinhauer & Deliyannis (2004), (5) Bond et al. 2017, (6) Paper I, (7) Cummings et al. (2017), (8) Lee-Brown et al. (2015), (9) Rich et al. (2013), (10) Malavolta et al. (2014). The photometric sources are (11) Johnson & Mitchell (1958), (12) Claria et al. (1998), (13) Kalirai et al. (2003), (14) Dachs (1970), (15) Sung et al. (2002), (16) Sung & Bessell (1999), (17) Johnson (1954), (18) Jones & Prosser (1996), (19) Ianna et al. (1987), (20) Sharma et al. (2006), (21) van Leeuwen (2007), (22) Ducati et al. (2001), (23) Fernandez & Salgado (1980), (24) Clem et al. (2011), (25) Kalirai et al. (2001b), (26) Cummings et al. (2017), (27) Kalirai et al. (2001a), (28) Kaluzny et al. (2013). See Cummings & Kalirai (2018) for discussion of the young cluster parameters. A single distance modulus is given because those measured with PARSEC and MIST models are indistinguishable.

5. White Dwarf Memberships in NGC 7789, NGC 6819, and NGC 6121

With the updated cluster reddenings, distance moduli, and white dwarf atmospheric parameters, it is appropriate to re-analyze the membership of the lower-mass white dwarfs from these three older clusters. As in our previous papers from this series, we compare each white dwarf's model-based intrinsic and observed photometry relative to the cluster's measured distance modulus and reddening, respectively.

In the upper panel of Figure 4 we plot the direct comparison of observed and model-based magnitudes (each white dwarf's apparent distance modulus) relative to the distance modulus of the cluster. The observed and model-based magnitude errors are added in quadrature (giving σ) and the white dwarf is deemed to have a consistent distance if its apparent distance modulus is within 2σ of the cluster's. The large sample of white dwarf members of NGC 6121, however, have a consistent but large systematically offset (0.28 mag) distance modulus from that photometrically measured with the main sequence. The white dwarf and main sequence photometry uses two different photometric sets that likely have systematic differences. Therefore, we take advantage of the large sample and define membership in NGC 6121 relative to this white dwarf-based distance modulus.

Similarly, in the lower panel of Figure 4, we plot a direct comparison of the observed and model-based $B-V$ colors (the apparent $E(B-V)$ reddening) relative to the derived cluster reddening for NGC 6819 and NGC 7789. For NGC 6121, the comparison uses $V-I$ colors and we adopt that $E(V-I) = 1.3 \times E(B-V)$. As with the distance moduli, the observed and model-based errors are added in quadrature (giving σ) and the reddenings are deemed consistent if they are within 2σ. Only white dwarf candidates that pass both photometric membership tests are adopted as likely single-star white dwarf members. In Table 3 the parameters of the white dwarfs consistent with single-star cluster membership are listed, but for brevity we do not list white dwarfs found inconsistent with membership and refer the reader to Kalirai et al. (2008, 2009) for more information on these likely non-members.

For memberships of the intermediate-mass white dwarfs in NGC 2099, these were analyzed in Papers I and III. With our additional signal on eight of these previously observed candidates from configuration F1, presented in Paper I, the additional signal does not affect the membership results. The same four remain consistent with membership (see Table 1), one remains inconsistent, and the last three still have signal too low to properly analyze.

For the higher-mass white dwarfs, we similarly analyzed their memberships in Papers II, and III, or adopted memberships from the references discussed in these papers. However, for higher-mass white dwarfs (e.g., $>0.8\ M_\odot$), the probability that a high-mass and recently formed white dwarf along the line of sight of a cluster is not a member is extremely unlikely. Therefore, we remain confident in their memberships.

6. The Initial–Final Mass Relation

The final step in deriving an IFMR is to apply the measured progenitor lifetimes to evolutionary models to infer each white dwarf's $M_{\rm initial}$. This is done by creating an isochrone at the progenitor's evolutionary lifetime and metallicity. Then the isochrone's given $M_{\rm initial}$ of a star at the tip of the AGB is the white dwarf's $M_{\rm initial}$. An advantage of using isochrones to measure cluster main sequence turnoff ages is that we self-consistently use the same evolutionary models for cluster ages and for estimating $M_{\rm initial}$. We note that here we use the non-rotating MIST isochrones to infer MIST-based $M_{\rm initial}$. In Figure 5 we display the PARSEC-based and MIST-based

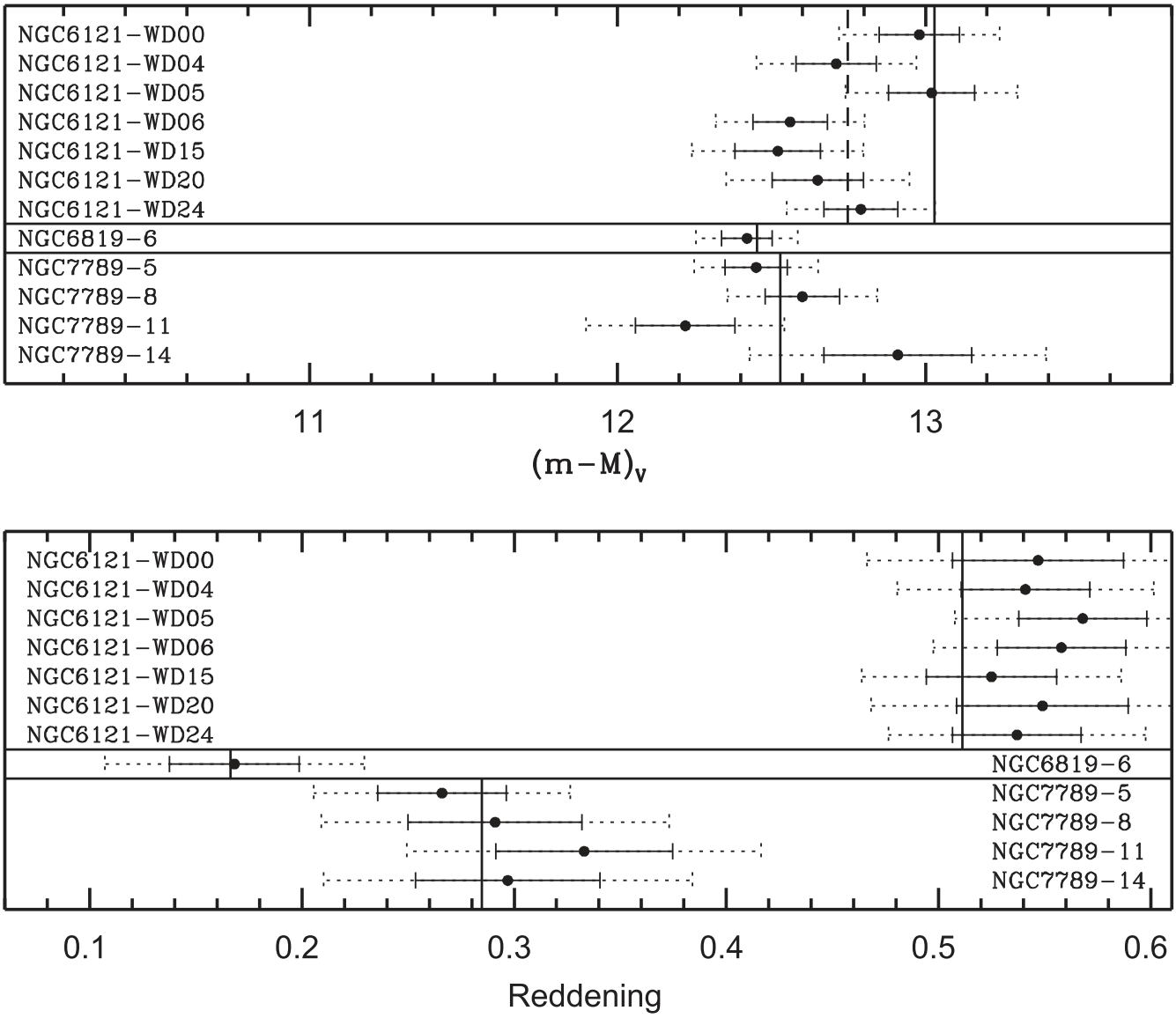

Figure 4. Upper panel: comparison of apparent distance modulus $(m - M)_V$ of each white dwarf vs. the cluster's photometric distance modulus in Figure 3 (shown as solid vertical lines). For NGC 6121, however, systematic issues in the photometry results in a clear systematic offset of the photometric distance modulus and the mean distance modulus of the white dwarf members shown as a dashed vertical line. The solid error bars represent the σ errors and the dashed error bars on 2σ errors. Lower panel: comparison of apparent reddening $E(V - I)$ for NGC 6121 and apparent $E(B - V)$ for NGC 6819 and NGC 7789. White dwarfs within 2σ of both the cluster distance modulus and reddening are adopted as single-star members.

IFMRs in the upper and lower panels, respectively. All white dwarf masses and inferred $M_{\rm initial}$ are given in Table 1.

Across the broad mass range of approximately 0.85 to 7.5 $M_\odot$, both the PARSEC-based and MIST-based IFMRs have minor scatter ($\sim$0.06 $M_\odot$) and are nonlinear. We define these IFMRs by fitting continuous three-piece relations. We acknowledge two outliers, NGC 2168-LAWDS11 and NGC 2099-WD33, which are not included in the fits, and are discussed in more detail in Papers II and III, respectively. In the following sections we discuss specific mass ranges of this semi-empirical IFMR.

6.1. The Low-mass IFMR

For white dwarf progenitors below 2 $M_\odot$, their derived $M_{\rm initial}$ are weakly sensitive to evolutionary lifetime (ages $>$1.34 Gyr). This results in the inferred $M_{\rm initial}$ being weakly sensitive to errors in cooling age and cluster age, and to the adopted evolutionary model. Additionally, the white dwarfs that have been observed in these older clusters are the brightest and most recently formed, which gives for each cluster no meaningful difference in their measured white dwarf masses or inferred $M_{\rm initial}$ values.

In Figure 5 we adopt a linear fit of the low-mass IFMR, but we will now look at the data trends more closely. The lowest-mass white dwarfs ($\sim$0.54 $M_\odot$) and their progenitors (0.83 $M_\odot$) are from the globular cluster NGC 6121. The IFMR then gradually increases to the single, but well measured, white dwarf from NGC 6819 at 0.60 $M_\odot$ and $M_{\rm initial} = 1.58\,M_\odot$. Moving to NGC 7789, the youngest of the three clusters, there is a rapid increase in its white dwarf masses (0.705 $M_\odot$) after only increasing to an $M_{\rm initial}$ of 1.82 $M_\odot$. These NGC 7789 white dwarfs are followed by a gap in the data, but their masses are consistent with the lowest-mass Hyades white dwarfs at a $M_{\rm initial}$ of $\sim$2.75 $M_\odot$.

Table 3
NGC 6121, NGC 6819, and NGC 7789 Likely Single-star Members

ID	α (J2000)	δ (J2000)	V (Obs.)	$V-I$ (Obs.)	V (Theory)	$V-I$ (Theory)
NGC 6121-WD00	16:23:49.90	−26:33:32.0	23.32 ± 0.05	0.32 ± 0.04	10.34 ± 0.12	−0.227 ± 0.005
NGC 6121-WD04	16:23:51.31	−26:33:04.0	22.69 ± 0.05	0.27 ± 0.03	9.98 ± 0.12	−0.271 ± 0.004
NGC 6121-WD05	16:23:41.38	−26:32:52.8	22.71 ± 0.05	0.27 ± 0.03	9.69 ± 0.13	−0.298 ± 0.003
NGC 6121-WD06	16:23:42.29	−26:32:39.1	22.65 ± 0.05	0.28 ± 0.03	10.09 ± 0.11	−0.278 ± 0.004
NGC 6121-WD15	16:23:51.00	−26:31:08.4	22.73 ± 0.05	0.26 ± 0.03	10.21 ± 0.13	−0.265 ± 0.006
NGC 6121-WD20	16:23:46.46	−26:30:32.4	23.01 ± 0.05	0.32 ± 0.04	10.36 ± 0.14	−0.229 ± 0.006
NGC 6121-WD24	16:23:41.18	−26:29:54.2	22.72 ± 0.05	0.26 ± 0.03	9.93 ± 0.11	−0.277 ± 0.004
ID	α (J2000)	δ (J2000)	V (Obs.)	$B-V$ (Obs.)	V (Theory)	$B-V$ (Theory)
NGC 6819-6	19:41:19.96	40:02:56.1	22.94 ± 0.02	0.07 ± 0.03	10.52 ± 0.08	−0.098 ± 0.006
NGC 7789-5	23:56:49.06	56:40:13.2	22.49 ± 0.01	0.04 ± 0.03	10.04 ± 0.10	−0.226 ± 0.004
NGC 7789-8	23:56:57.22	56:40:01.1	23.15 ± 0.02	0.15 ± 0.04	10.55 ± 0.12	−0.141 ± 0.009
NGC 7789-11	23:56:30.81	56:37:19.3	23.36 ± 0.02	0.27 ± 0.04	11.14 ± 0.16	−0.063 ± 0.012
NGC 7789-14	23:56:37.78	56:39:08.4	23.55 ± 0.02	0.21 ± 0.04	10.64 ± 0.24	−0.087 ± 0.017

Theoretical models at these lower masses, in general, predict slowly increasing white dwarf mass with increasing $M_{\rm initial}$ (e.g., Meng et al. 2008; Choi et al. 2016). In Figure 5 we plot the IFMR data in comparison to the theoretical IFMR at the solar metallicity of Choi et al. (2016) in dashed blue. The trend between the NGC 6121 and NGC 6819 white dwarfs is comparable with this model, but the NGC 7789 white dwarfs begin to diverge to relatively higher masses. Figure 5 also compares to the solar-metallicity theoretical IFMR of Marigo & Girardi (2007), which illustrates some of the variation of theoretical IFMRs at these masses. This results from the final white dwarf mass having large sensitivity to adopted mass-loss rates and third dredge-up at these masses. The Marigo & Girardi (2007) model more closely follows the observed IFMR trends at these low masses, followed by a plateau up to the Hyades white dwarfs at $M_{\rm initial} = 2.75\,M_{\odot}$, but the gaps in data and the broad range of metallicity for these older clusters currently limit the ability to further constrain these models.

White dwarfs from clusters with ages between the Hyades (700 Myr) and NGC 7789 (1.5 Gyr) will be valuable to fill in this broad gap from 1.82 to 2.75 $M_{\odot}$. However, the observed field white dwarf mass distribution (e.g., Tremblay et al. 2016) can provide insight on the IFMR's general characteristics in this gap. For example, a rapid increase of white dwarf masses in the IFMR, as seen between NGC 6819 and NGC 7789, followed by a plateau at $\sim$0.7 $M_{\odot}$, from 1.82 to 2.75 $M_{\odot}$, would produce the established mass distribution peak at $\sim$0.6 $M_{\odot}$ but it would be followed by a sharp drop in number at masses near 0.65 $M_{\odot}$ and a strong secondary peak near 0.7 $M_{\odot}$. Such features are not observed in the SDSS field white dwarf sample (e.g., Kepler et al. 2016) or *Gaia* DR2 data (Gaia Collaboration et al. 2018a).

This field white dwarf comparison does not contradict the observed jump in white dwarf masses in NGC 7789, but it suggests that it could be a result of NGC 7789's subsolar metallicity. We also cannot know for certain that the IFMR is monotonic within this gap. Instead of a plateau at 0.7 $M_{\odot}$, it is possible that the white dwarf masses may decrease and then rise again between progenitors of 1.82 to 2.75 $M_{\odot}$. This would more evenly distribute the white dwarf masses in the field and such a trend could result from this region's strong sensitivity to third dredge-up efficiency and mass loss during the TP-AGB.

6.2. Intermediate and High-mass IFMR

In Papers I, II, and III we presented 35 intermediate-mass white dwarfs (those with progenitors from 2.75 to 4 $M_{\odot}$). These include all of the white dwarfs consistent with membership in the Hyades and Praesepe, all but NGC 2099-WD33 in NGC 2099, and the four lowest-mass NGC 3532 white dwarfs. The new Keck I LRIS observations have acquired additional signal on four NGC 2099 white dwarf members. Here, for the first time, we have also analyzed all of these intermediate-mass white dwarfs and their clusters self-consistently using the methods introduced in Paper II. Both this consistency and increased signal further strengthen that in this region the IFMR slope is increased by a factor of $\sim$2 relative to the higher and lower masses.

The differences in PARSEC- and MIST-based $M_{\rm initial}$ values remain minor (within 5%) up to progenitors near 5 $M_{\odot}$. Above these masses the MIST models infer increasingly lower masses compared to the PARSEC models. This shows the increased sensitivity of inferred $M_{\rm initial}$ to evolutionary lifetime at these higher masses. These white dwarfs with high-mass progenitors are all from the Pleiades, the youngest cluster analyzed here (130 Myr). Cummings & Kalirai (2018) showed that the non-rotating MIST and PARSEC isochrones begin to significantly underestimate ages for cluster younger than 100 Myr. For the marginally older Pleiades the non-rotating MIST isochrones measure an age of 135 Myr, consistent with the reliable lithium depletion boundary age (130 Myr) and the rotating SYCLIST isochrone age (125 Myr). However, the non-rotating PARSEC isochrones still give a younger Pleiades age (115 Myr), giving that the PARSEC models will likely overestimate the Pleiades progenitor masses. Therefore, MIST-based progenitor masses are better founded and will provide our adopted $M_{\rm initial}$ values.

To define the semi-empirical IFMR, we linearly fit the relation above and below the second dredge-up turnover, which based on these data we determine to be at 3.60 $M_{\odot}$. We have also linearly fit the low-mass white dwarf region. We require these relations to be continuous and this gives a set of three equations for both the PARSEC and MIST-based IFMR, which

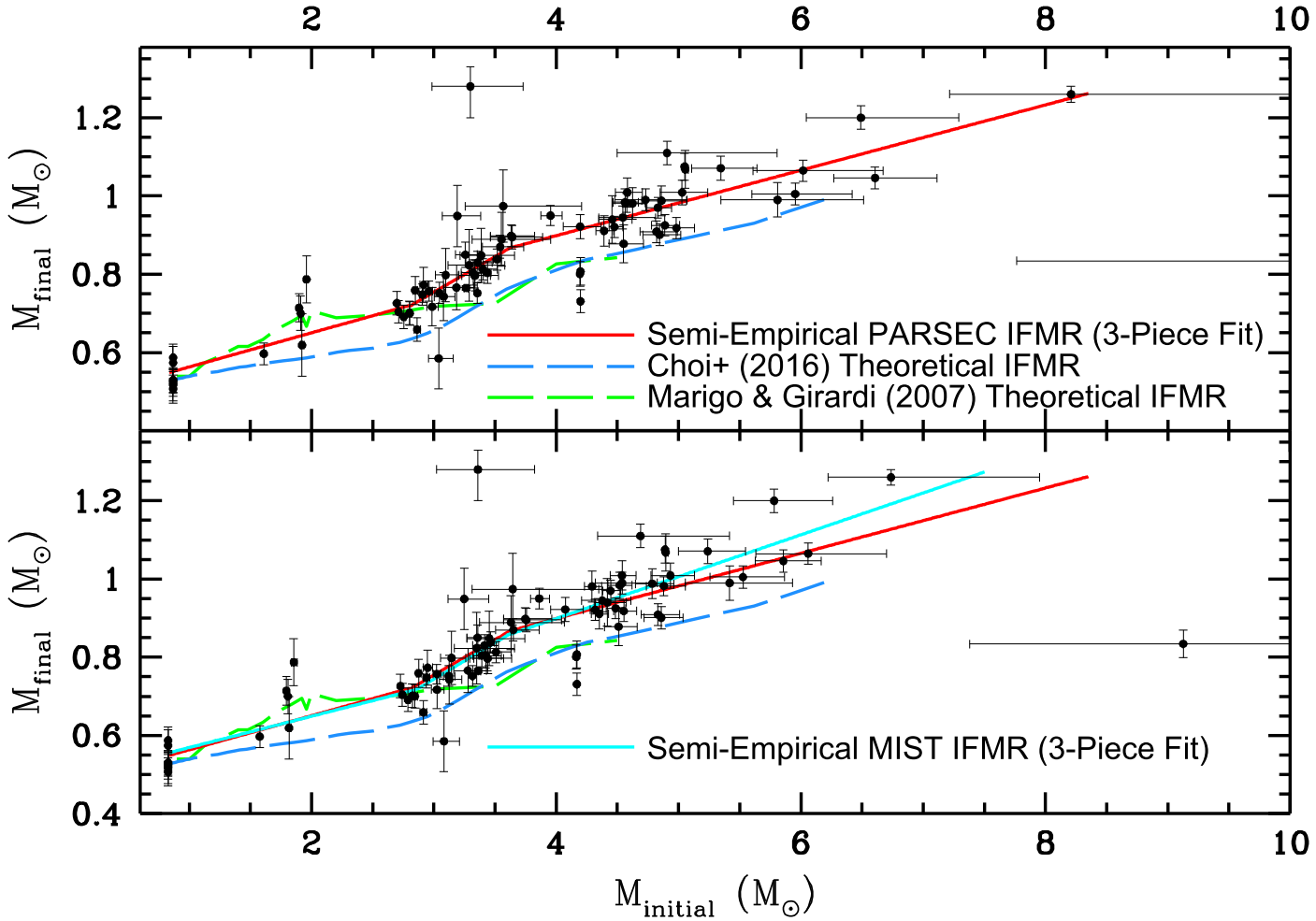

Figure 5. Upper panel: PARSEC-based IFMR data in black. The semi-empirical trend is in three pieces and is shown in red. The data are also compared to the theoretical IFMR from Choi et al. (2016) for non-rotating stars in dashed blue. The observed data show a remarkably consistent shape, but at intermediate and higher masses there is a systematic offset with the observed white dwarfs having masses ~0.1 $M_\odot$ higher than theory predicts. Lower panel: comparable MIST-based IFMR data in black. A similar three-piece fit to this semi-empirical data in shown in cyan, with the same three-piece relation from the upper panel shown in red for comparison. These relations are consistent at lower and intermediate masses, but at high masses they begin to diverge with increasing mass. This also increases the systematic difference between the MIST-based IFMR and model at the highest masses.

is our adopted IFMR. Note the defined $M_{\rm initial}$ ranges for each equation and that the slope and y-intercept errors are correlated:

PARSEC-Based IFMR[9]

$$M_{\rm f} = (0.0873 \pm 0.0190) \times M_{\rm i} + (0.476 \pm 0.033) M_\odot \quad (0.87 M_\odot < M_{\rm i} < 2.80 M_\odot) \quad (1)$$

$$M_{\rm f} = (0.181 \pm 0.041) \times M_{\rm i} + (0.210 \pm 0.131) M_\odot \quad (2.80 M_\odot < M_{\rm i} < 3.65 M_\odot) \quad (2)$$

$$M_{\rm f} = (0.0835 \pm 0.0144) \times M_{\rm i} + (0.565 \pm 0.073) M_\odot \quad (3.65 M_\odot < M_{\rm i} < 8.20 M_\odot) \quad (3)$$

MIST-Based IFMR (Our Adopted IFMR)

$$M_{\rm f} = (0.080 \pm 0.016) \times M_{\rm i} + (0.489 \pm 0.030) M_\odot \quad (0.83 M_\odot < M_{\rm i} < 2.85 M_\odot) \quad (4)$$

$$M_{\rm f} = (0.187 \pm 0.061) \times M_{\rm i} + (0.184 \pm 0.199) M_\odot \quad (2.85 M_\odot < M_{\rm i} < 3.60 M_\odot) \quad (5)$$

$$M_{\rm f} = (0.107 \pm 0.016) \times M_{\rm i} + (0.471 \pm 0.077) M_\odot \quad (3.60 M_\odot < M_{\rm i} < 7.20 M_\odot). \quad (6)$$

There remains moderate dispersion in the semi-empirical data surrounding these relations. When excluding the NGC 2099-WD33 and NGC 2168-LAWDS11 outliers, the standard deviations in both IFMRs are 0.06 $M_\odot$. This scatter is approximately half of that observed in the previous semi-empirical IFMRs of Catalán et al. (2008b) and Salaris et al. (2009) also excluding NGC 2168–LAWDS11). This illustrates the advantage of self-consistent analysis of both the star clusters and white dwarfs. The remaining scatter in this semi-empirical IFMR is also consistent with the observational errors at lower and intermediate masses (<4 $M_\odot$), but at higher masses the scatter is increasingly larger than expected based on the errors alone.

In Figure 5, the comparisons of the entire mass range to the theoretical IFMR of Choi et al. (2016) finds remarkable agreement in the IFMR slope at intermediate masses, and there is a consistent turnover in the IFMR in both observations and theory near an $M_{\rm initial}$ of 3.5–4 $M_\odot$. At higher masses the slope of the PARSEC-based IFMR also remains consistent with the model, but the MIST-based IFMR is moderately steeper here.

[9] For comparison, the high-mass PARSEC-based IFMR equation from Paper II has a typographical error. The published IFMR slope should have been 0.0907 instead of 0.097.

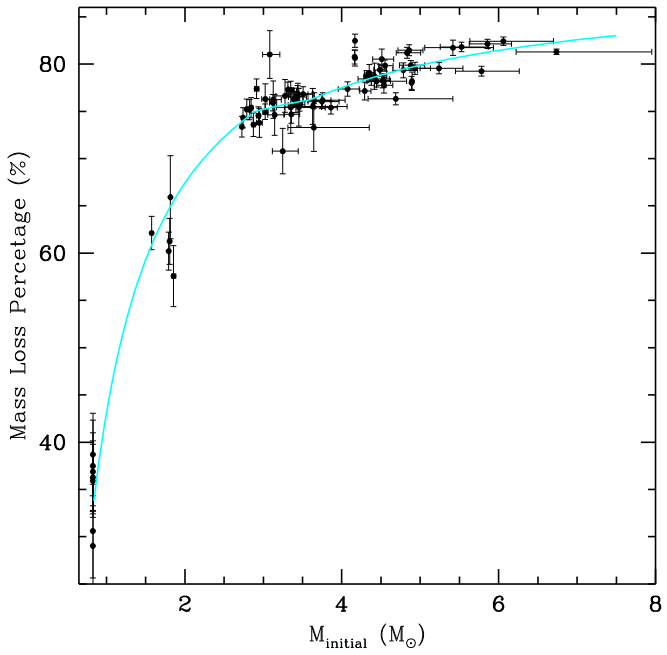

Figure 6. From the MIST-based IFMR we plot the total mass loss that occurs throughout a star's lifetime as a percentage of its $M_{\rm initial}$. This mass loss ranges from 33% at $M_{\rm initial}$ of 0.83 $M_{\odot}$ to 83% at $M_{\rm initial}$ of 7.5. The trend in cyan is a direct conversion of the relation shown in cyan in the lower panel of Figure 5.

For both semi-empirical IFMRs, there is a systematic offset of $\sim$0.1 $M_{\odot}$ which remains nearly uniform across this entire broad range of masses from progenitors of 3–6 $M_{\odot}$.

6.3. Total Mass Loss

We can quantify the strong sensitivity of total mass loss to the $M_{\rm initial}$ of a star. In Figure 6 we apply the MIST-based IFMR to calculate the total integrated mass loss that occurs during a star's lifetime as a percentage of its $M_{\rm initial}$. This shows that at $M_{\rm initial} = 0.83\,M_{\odot}$ a star will lose 33% of its total mass throughout its lifetime. With increasing progenitor mass this percentage rapidly increases to 60% at $M_{\rm initial} = 1.5\,M_{\odot}$, and then 80% at $M_{\rm initial} = 5\,M_{\odot}$. The GD50 white dwarf has the most massive progenitor analyzed here at $6.74\,M_{\odot}$, and it lost a notable 81.5% of its initial mass throughout its life (5.48 $M_{\odot}$ total). Figure 6 gives us a quantitative understanding of how evolution of a star will directly affect its surroundings and how evolution of low-mass stars has only a moderate effect on their resulting gravity, but higher-mass stars will significantly change their gravity throughout their evolution. This will have important effects on their dynamics in clusters and on any planets and material in orbit around these stars.

The sensitivity of this total mass loss to metallicity remains poorly understood and with little observational constraint. In Paper I we compared the intermediate-mass IFMR of the solar metallicity NGC 2099 to the metal-rich ([Fe/H] = +0.15) Hyades and Praesepe and found that this moderate metallicity difference had no detectable effect on total mass loss. We can now look at this further with this larger sample and expanded mass and metallicity range. If the metallicity differences between the intermediate and young clusters ($-0.15 <$ [Fe/H] $< +0.15$) had a detectable effect on mass loss, it would result in systematic shifts in the IFMR that correlate with [Fe/H] (see cluster [Fe/H] in Table 2). We test this using residuals from the observed white dwarf masses relative to the fits in Equations (5) and (6). This test requires that at a given $M_{\rm initial}$ there are data across a broad range of [Fe/H]. Otherwise, any effects of metallicity will directly affect the fit itself and remove any metallicity-dependent residuals. This [Fe/H] range is provided at intermediate and high masses, but for this reason we do not consider the low-mass white dwarfs ($M_{\rm initial} < 2$).

Consistent with Paper I there is no detectable metallicity dependence across the range of $0 <$ [Fe/H] $< +0.15$ for stars from 2.75 to 4 $M_{\odot}$. There is also no detectable metallicity dependence across the range of $-0.15 <$ [Fe/H] $< +0.04$ for stars from 4 $M_{\odot}$ to 6 $M_{\odot}$. Observational evidence for the metallicity dependence of mass loss remains elusive, but when considering observational errors this metallicity effect is likely too small to detect across this moderate metallicity range. Intermediate- and high-mass white dwarfs (>0.7 $M_{\odot}$) from clusters at either high or low metallicity would provide a remarkable test of this dependence, but such clusters are more distant and their higher-mass white dwarfs are beyond current spectroscopic limitations.

7. Summary and Conclusions

In this paper we have expanded the uniform analysis of the IFMR for $M_{\rm initial}$ from 0.85 to 7.5 $M_{\odot}$. We have analyzed open cluster photometry for NGC 6121, NGC 6819, NGC 7789, Praesepe, the Hyades, and NGC 2099, and we have re-analyzed their white dwarf data and, when appropriate, their memberships. We have acquired more signal with Keck I LRIS for four of NGC 2099 white dwarfs near the IFMR turnover at $M_{\rm initial} \sim 3.65\,M_{\odot}$. To extend to higher masses, we have also similarly analyzed the available spectroscopic data for the three massive white dwarfs in the young open cluster NGC 1039. This produces the most complete semi-empirical IFMR available.

By comparing the PARSEC- and MIST-based IFMRs, we have also tested the sensitivity of the derived white dwarf progenitor masses to the applied stellar evolutionary model. We find both IFMRs are reassuringly very similar at all but the highest $M_{\rm initial}$ (>5.5 $M_{\odot}$). This difference is due to the sensitivity of inferred $M_{\rm initial}$ to evolutionary lifetime increasing significantly, and to non-rotating PARSEC isochrones underestimating the Pleiades age, but even here the differences between the progenitor masses for fit IFMRs remain within 1 $M_{\odot}$. The consistency at all other mass ranges shows the importance of using the same evolutionary model to both determine the cluster age and to infer the $M_{\rm initial}$ from the resulting evolutionary lifetime.

Using this MIST-based IFMR to constrain mass loss shows that at progenitors of 0.83 $M_{\odot}$ a star will lose 33% of its $M_{\rm initial}$ throughout its evolution, but this mass loss percentage increases rapidly with increasing $M_{\rm initial}$, reaching 83% of $M_{\rm initial}$ being lost for progenitors at 7.5 $M_{\odot}$. Testing these mass loss data further finds they have no meaningful sensitivity to metallicity for intermediate- and high-mass white dwarfs throughout the moderate metallicity range of the analyzed clusters ($-0.15 <$ [Fe/H] $< +0.15$).

This IFMR can further be used as a valuable constraint to models of single-star stellar evolution that consider all phases. This semi-empirical IFMR is consistent at the lowest masses ($M_{\rm initial} \sim 0.85\,M_{\odot}$) with the models (e.g., Marigo & Girardi 2007; Meng et al. 2008; Choi et al. 2016). At higher masses the observed data suggest a more rapid increase in white dwarf masses (to 0.7 $M_{\odot}$) than most theoretical models predict.

Following this there is a large gap in progenitor data from 1.85 to 2.75 $M_{\odot}$ with no apparent change in white dwarf masses. A simple plateau in the IFMR could occur here, but we note that such a plateau would result in a significant overproduction of $\sim$0.7 $M_{\odot}$ white dwarfs that is not observed in the field. A more complicated trend may exist within this gap, including mass ranges where white dwarf mass decreases with increasing $M_{\rm initial}$.

For intermediate and higher masses, the consistency between the theoretical IFMRs is compelling, where all predict a steeper IFMR slope in intermediate masses followed by a turnover to a shallower slope beginning near 3.5–4 $M_{\odot}$. Such a trend is similarly observed in the data, but for progenitors from 3 to 6 $M_{\odot}$ there is a systematic offset with the semi-empirical IFMR having white dwarfs $\sim$0.1 $M_{\odot}$ more massive than theoretical models predict. This offset may indicate limitations in how these models address, for example, mass loss and third dredge-up efficiency. In our upcoming paper we will consider these factors and address the important sensitivity that the semi-empirical IFMR can have to progenitor rotation.

This project was supported by the National Science Foundation (NSF) through grant AST-1614933. Data presented herein were obtained at the WM Keck Observatory from telescope time allocated to the National Aeronautics and Space Administration through the agency's scientific partnership with the California Institute of Technology and the University of California. The Observatory was made possible by the generous financial support of the WM Keck Foundation. This research has made use of the WEBDA database, operated at the Department of Theoretical Physics and Astrophysics of the Masaryk University.

This work has made use of data from the European Space Agency (ESA) mission *Gaia* (https://www.cosmos.esa.int/gaia), processed by the *Gaia* Data Processing and Analysis Consortium (DPAC, https://www.cosmos.esa.int/web/gaia/dpac/consortium). Funding for the DPAC has been provided by national institutions, in particular the institutions participating in the *Gaia* Multilateral Agreement.

ORCID iDs

Jeffrey D. Cummings https://orcid.org/0000-0001-7453-9947
Jason S. Kalirai https://orcid.org/0000-0001-9690-4159
P.-E. Tremblay https://orcid.org/0000-0001-9873-0121
Enrico Ramirez-Ruiz https://orcid.org/0000-0003-2558-3102
Jieun Choi https://orcid.org/0000-0002-8822-1355

References

Althaus, L. G., García-Berro, E., Isern, J., Córsico, A. H., & Rohrmann, R. D. 2007, A&A, 465, 249
Andrews, J. J., Agüeros, M. A., Gianninas, A., et al. 2015, ApJ, 815, 63
Anthony-Twarog, B. J., Deliyannis, C. P., & Twarog, B. A. 2014, AJ, 148, 51
Bergeron, P., Saffer, R. A., & Liebert, J. 1992, ApJ, 394, 228
Bond, H. E., Schaefer, G. H., Gilliland, R. L., et al. 2017, ApJ, 840, 70
Bressan, A., Marigo, P., Girardi, L., et al. 2012, MNRAS, 427, 127
Camisassa, M. E., Althaus, L. G., Córsico, A. H., et al. 2018, arXiv:1807.03894
Casewell, S. L., Dobbie, P. D., Napiwotzki, R., et al. 2009, MNRAS, 395, 1795
Catalán, S., Isern, J., García-Berro, E., et al. 2008a, A&A, 477, 213
Catalán, S., Isern, J., García-Berro, E., & Ribas, I. 2008b, MNRAS, 387, 1693
Choi, J., Dotter, A., Conroy, C., et al. 2016, ApJ, 823, 102
Claria, J. J., Piatti, A. E., & Lapasset, E. 1998, A&A, 128, 131
Clem, J. L., Landolt, A. U., Hoard, D. W., & Wachter, S. 2011, AJ, 141, 115
Cummings, J. 2011, PhD thesis, Indiana Univ.—Bloomington
Cummings, J. D. 2017, in IAU Symp. 323, Planetary Nebulae: Multi-Wavelength Probes of Stellar and Galactic Evolution, ed. X. Liu, L. Stanghellini, & A. Karakas (Cambridge: Cambridge Univ. Press), 157
Cummings, J. D., Deliyannis, C. P., Maderak, R. M., & Steinhauer, A. 2017, AJ, 153, 128
Cummings, J. D., & Kalirai, J.-S. 2018, AJ, 156, 165
Cummings, J. D., Kalirai, J. S., Tremblay, P.-E., & Ramirez-Ruiz, E. 2015, ApJ, 807, 90
Cummings, J. D., Kalirai, J. S., Tremblay, P.-E., & Ramirez-Ruiz, E. 2016a, ApJ, 818, 84
Cummings, J. D., Kalirai, J. S., Tremblay, P.-E., Ramirez-Ruiz, E., & Bergeron, P. 2016b, ApJL, 820, L18
Dachs, J. 1970, A&A, 5, 312
de Bruijne, J. H. J., Hoogerwerf, R., & de Zeeuw, P. T. 2001, A&A, 367, 111
Dobbie, P. D., Day-Jones, A., Williams, K. A., et al. 2012, MNRAS, 423, 2815
Dobbie, P. D., Napiwotzki, R., Burleigh, M. R., et al. 2009, MNRAS, 395, 2248
Dobbie, P. D., Napiwotzki, R., Lodieu, N., et al. 2006, MNRAS, 373, L45
Doherty, C. L., Gil-Pons, P., Siess, L., Lattanzio, J. C., & Lau, H. H. B. 2015, MNRAS, 446, 2599
Dotter, A. 2016, ApJ, 222, 8
Dotter, A., Conroy, C., Cargile, P., & Asplund, M. 2017, ApJ, 840, 99
Ducati, J. R., Bevilacqua, C. M., Rembold, S. B., & Ribeiro, D. 2001, ApJ, 558, 309
El-Badry, K., Rix, H.-W., & Weisz, D. R. 2018, ApJL, 860, L17
Fernandez, J. A., & Salgado, C. W. 1980, A&A, 39, 11
Fernie, J. D. 1963, AJ, 68, 780
Finley, D. S., & Koester, D. 1997, ApJL, 489, L79
Fontaine, G., Brassard, P., & Bergeron, P. 2001, PASP, 113, 409
Gagné, J., Fontaine, G., Simon, A., & Faherty, J. K. 2018, ApJL, 861, L13
Gaia Collaboration, Babusiaux, C., van Leeuwen, F., et al. 2018a, arXiv:1804.09378
Gaia Collaboration, Brown, A. G. A., Vallenari, A., et al. 2018b, arXiv:1804.09365
Gaia Collaboration, Prusti, T., de Bruijne, J. H. J., et al. 2016, A&A, 595, A1
Gray, D. F. 2014, AJ, 147, 81
Hubeny, I. 1988, CoPhC, 52, 103
Hubeny, I., Blaes, O., Krolik, J. H., & Agol, E. 2001, ApJ, 559, 680
Hubeny, I., & Lanz, T. 1995, ApJ, 439, 875
Ianna, P. A., Adler, D. S., & Faudree, E. F. 1987, AJ, 93, 347
Johnson, H. L. 1954, ApJ, 119, 185
Johnson, H. L., & Mitchell, R. I. 1958, ApJ, 128, 31
Jones, B. F., & Prosser, C. F. 1996, AJ, 111, 1193
Kalirai, J. S., Bergeron, P., Hansen, B. M. S., et al. 2007, ApJ, 671, 748
Kalirai, J. S., Fahlman, G. G., Richer, H. B., & Ventura, P. 2003, AJ, 126, 1402
Kalirai, J. S., Hansen, B. M. S., Kelson, D. D., et al. 2008, ApJ, 676, 594
Kalirai, J. S., Marigo, P., & Tremblay, P.-E. 2014, ApJ, 782, 17
Kalirai, J. S., Richer, H. B., Fahlman, G. G., et al. 2001a, AJ, 122, 266
Kalirai, J. S., Richer, H. B., Reitzel, D., et al. 2005, ApJL, 618, L123
Kalirai, J. S., Saul Davis, D., Richer, H. B., et al. 2009, ApJ, 705, 408
Kalirai, J. S., Ventura, P., Richer, H. B., et al. 2001b, AJ, 122, 3239
Kaluzny, J., Thompson, I. B., Rozyczka, M., & Krzeminski, W. 2013, AcA, 63, 181
Kepler, S. O., Pelisoli, I., Koester, D., et al. 2016, MNRAS, 455, 3413
Lee-Brown, D. B., Anthony-Twarog, B. J., Deliyannis, C. P., Rich, E., & Twarog, B. A. 2015, AJ, 149, 121
Liebert, J., Bergeron, P., & Holberg, J. B. 2005, ApJ, 156, 47
Luhman, K. L., Stauffer, J. R., & Mamajek, E. E. 2005, ApJL, 628, L69
Malavolta, L., Sneden, C., Piotto, G., et al. 2014, AJ, 147, 25
Marigo, P., & Girardi, L. 2007, A&A, 469, 239
Meng, X., Chen, X., & Han, Z. 2008, A&A, 487, 625
Miglio, A., Brogaard, K., Stello, D., et al. 2012, MNRAS, 419, 2077
Netopil, M., Paunzen, E., Heiter, U., & Soubiran, C. 2016, A&A, 585, A150
Oke, J. B., Cohen, J. G., Carr, M., et al. 1995, PASP, 107, 375
Ortega, V. G., Jilinski, E., de La Reza, R., & Bazzanella, B. 2007, MNRAS, 377, 441
Paxton, B., Bildsten, L., Dotter, A., et al. 2011, ApJ, 192, 3
Paxton, B., Cantiello, M., Arras, P., et al. 2013, ApJ, 208, 4
Paxton, B., Marchant, P., Schwab, J., et al. 2015, ApJ, 220, 15
Raddi, R., Catalán, S., Gänsicke, B. T., et al. 2016, MNRAS, 457, 1988

Rich, E., Anthony-Twarog, B. J., Deliyannis, C. P., & Twarog, B. A. 2013, AAS Meeting, 221, 250.27
Rubin, K. H. R., Williams, K. A., Bolte, M., & Koester, D. 2008, AJ, 135, 2163
Salaris, M., Serenelli, A., Weiss, A., & Miller Bertolami, M. 2009, ApJ, 692, 1013
Schuler, S. C., Plunkett, A. L., King, J. R., & Pinsonneault, M. H. 2010, PASP, 122, 766
Sharma, S., Pandey, A. K., Ogura, K., et al. 2006, AJ, 132, 1669
Steinhauer, A., & Deliyannis, C. P. 2004, ApJL, 614, L65
Sung, H., & Bessell, M. S. 1999, MNRAS, 306, 361
Sung, H., Bessell, M. S., Lee, B.-W., & Lee, S.-G. 2002, AJ, 123, 290
Tremblay, P.-E., & Bergeron, P. 2009, ApJ, 696, 1755
Tremblay, P.-E., Bergeron, P., & Gianninas, A. 2011, ApJ, 730, 128
Tremblay, P.-E., Cummings, J., Kalirai, J. S., et al. 2016, MNRAS, 461, 2100
Tremblay, P.-E., Ludwig, H.-G., Steffen, M., & Freytag, B. 2013, A&A, 559, A104
Twarog, B. A., Anthony-Twarog, B. J., & Schafer, B. S. 2012, AAS Meeting, 219, 438.09
van Leeuwen, F. 2007, A&A, 474, 653
Weidemann, V. 1977, A&A, 59, 411
Weidemann, V. 2000, A&A, 363, 647
Williams, K. A., Bolte, M., & Koester, D. 2009, ApJ, 693, 355
Williams, K. A., Canton, P. A., Bellini, A., et al. 2018, arXiv:1807.09315
Yi, S., Demarque, P., Kim, Y.-C., et al. 2001, ApJ, 136, 417
Zhao, J. K., Oswalt, T. D., Willson, L. A., Wang, Q., & Zhao, G. 2012, ApJ, 746, 144